Investigation on polyethylene glycol assisted solvothermal synthesis of $CuCoO_2$ nanosheets for efficient oxygen evolution reaction

Shiyu Ma,[a] Jilin Bai,[a] Li Sun,[a] Lihong Zhao,[a] Hao Tan,[a,b] Lifeng Liu,[b] Zhigang Peng,[c] Xiujian Zhao,[a] and Dehua Xiong*,[a]*

a. State Key Laboratory of Silicate Materials for Architectures, Wuhan University of Technology, Wuhan 430070, P. R. China.
b. Songshan Lake Materials Laboratory, Dongguan, 523808, P. R. China.
c. Shahe Glass Technology Research Institute of Hebei Province, Xingtai 054000, P. R. China.

* Corresponding author email:
baijilin520@whut.edu.cn (J. Bai), xiongdehua2010@gmail.com (D. Xiong).

Experimental details

Materials synthesis

All chemicals in the experiment were of analytical grade without further purification. Cu-BTC and $CuCoO_2$ were prepared according to our previous work. [1]

Cu-BTC synthesis: Firstly, 2.6093 g $Cu(NO_3)_2 \cdot 3H_2O$, 1.2600 g H_3BTC and 9 mL isopropyl alcohol (IPA) were dissolved in 27 mL deionized (DI) water and 36 mL absolute ethanol (ET), and magnetically stirring for 30 minutes. Secondly, the solution was transferred into a 100 mL Teflon lined autoclave and kept at 120 °C for hydrothermal reaction for 12 h. Afterwards, the resulting blue precipitate was washed three times with ET to remove any by-product impurities. Finally, the Cu-BTC was dried at 70 °C for 5 h for further use.

$CuCoO_2$ synthesis: Firstly, 1.50 g Cu-BTC, 1.60 g $Co(NO_3)_2 \cdot 6H_2O$ and 1.40 g NaOH were dissolved in DI water and ET (or DI water and polyethylene glycol (PEG-400)), and magnetically stirring for 30 minutes. Secondly, the surfactant was added to the above solution and stirred for 1 h. Afterwards, the solution was transferred into a 100 mL Teflon lined autoclave and kept at 140 °C for hydrothermal reaction for 24 h. Finally, the obtained precipitate was washed several times with ammonia, DI water, and ET, and then dried at 70 °C for 5 h for further characterization.

Structural characterization

The crystal phase of samples was characterized by the X-ray diffraction (XRD, D8 Advance, Bruker, Germany). The morphology, microstructure, and chemical composition of the samples were examined by field-emission scanning electron microscopy (FESEM, Sigma 300, Zeiss, Germany) and transmission electron microscopy (TEM, JEM-2100 operating at 200 keV, JEOL, Japan) equipped with energy-dispersive X-ray spectroscopy (EDS). An atomic force microscopy (AFM) with DI Nanoscope IV controller (SPA400, NSK Ltd., Japan) was used to record the AFM height images of the sample. The surface chemical states of the samples were analyzed by X-ray photoelectron spectroscopy (XPS, Escalab 250Xi, Thermo Fisher Scientific,

USA). The C 1s line (284.80 eV) corresponding to the surface adventitious carbon (C-C line bond) has been used as the reference binding energy. The structure of samples was investigated by Raman (LABHRev-UV, HORIBA Jobin Yvon, France) and Fourier Transform Infrared (Nicolet 6700, Thermo Fisher Scientific, USA). The Brunauer-Emmett-Teller (BET) specific surface areas and porosity parameters of the samples were taken by N_2 adsorption-desorption isothermetry (TriStar II 3020, Micromeritics, USA).

Electrode preparation and electrochemical measurement

Firstly, 15.0 mg $CuCoO_2$ was dissolved in 500 μL DI water, 480 μL IPA and 20 μL Nafion (5 wt%, Sigma) to make a suspension, then 20 μL of the suspension solution was placed on Ni foam (1 cm×1 cm), and finally the working electrode was prepared by drying at 150 °C for 10 min. The working electrodes prepared with CCO1 and CCO2 were named Ni@CCO1 and Ni@CCO2, respectively.

The OER performance was evaluated by cyclic voltammetry (CV) and electrochemical impedance spectroscopy (EIS) in a three-electrode configuration in 1.0 M KOH (pH = 13.5) using a CS2350H electrochemical workstation (Wuhan Corrtest Instruments Corp., China). A platinum wire and a saturated calomel electrode (SCE) were used as the counter and reference electrodes, respectively. Cyclic voltammetric (CV) scans were recorded between 1.05 and 1.80 V vs. reversible hydrogen electrode (RHE) at a scan rate of 2 $mV \cdot s^{-1}$. The electrochemical double-layer capacitance (C_{dl}) can be extracted through CV scans recorded at different rates (from 20 to 100 $mV \cdot s^{-1}$) in the non-faradaic potential window of -0.05-0.05 V vs. SCE. The EIS measurements were performed in the frequency range of 100 kHz-10 mHz under a constant potential of 1.63 V vs. RHE. Under the constant current density of 10 mA cm^{-2}, the stability of the sample was tested for 18 hours.

All current density values are normalized with respect to the geometrical surface area of the working electrode. All CV curves presented in this work are *iR*-corrected (85%). The correction was done according to the following equation:

$$E_c = E_m - iR_s \quad \text{(S1)}$$

where E_c is the *iR*-corrected potential, E_m experimentally measured potential, and R_s the equivalent series resistance extracted from the electrochemical impedance spectroscopy measurements. Unless otherwise specified, all potentials are reported versus reversible hydrogen electrode (RHE) by converting the potentials measured vs. SCE according to the following formula:

$$E\,(\mathrm{RHE}) = E\,(\mathrm{SCE}) + 0.241 + 0.059\,\mathrm{pH} \qquad (S2)$$

Supplementary tables:

Table S1. Detailed reaction conditions were employed to synthesize delafossite $CuCoO_2$ nanocrystals.

No.	Cu-BTC (g)	$Co(NO_3)_2$ (g)	NaOH (g)	Surfactant		Solvent (mL)	Temp. (℃)	Time (h)
				type	content (mmol)			
1	1.50	1.60	1.40	SDS	5	50 ET：20 DI	140	24
2					10			
3					15			
4				CTAB	5			
5					10			
6					15			
7				PVP	20			
8					30			
9					40			
10				PVP	30	50 PEG：20 DI		
11						40 PEG：30 DI		
12						30 PEG：40 DI		
13						20 PEG：50 DI		
14						10 PEG：60 DI		

Table S2. The OER performance of these electrodes in this work compared with other oxide catalysts.

Catalyst	Electrolyte	η_{10} (mV)	Tafel slope (mV dec^{-2})	(year)[Ref.]
Bare Ni	1.0 M KOH	495	135	This work
Ni@CCO1		415	99	
Ni@CCO2		378	85	
$CuCoO_2$		390	70	(2018)[2]
Ni doped $CuCoO_2$		409	98	(2022)[3]
Fe doped $CuCoO_2$		369	69	(2023)[1]
Ca doped $CuCoO_2$		470	96.5	(2020)[4]
$CuGaO_2$		400	61	(2022)[5]
$AgCoO_2$		395		(2019)[6]
$AgCoO_2$/Ag		271		(2019)[6]
AgFeO2		400	84	(2019)[7]
$La_{0.9}Sn_{0.1}NiO_{3-\delta}$		318	74	(2022)[8]
$La_{1-x}Sr_xCoO_{3-\delta}$		326	70.8	(2018)[9]
$LaFeO_3$		420	62	(2019)[10]
$LaNiO_3$		460	96	(2021)[11]

Supplementary figures:

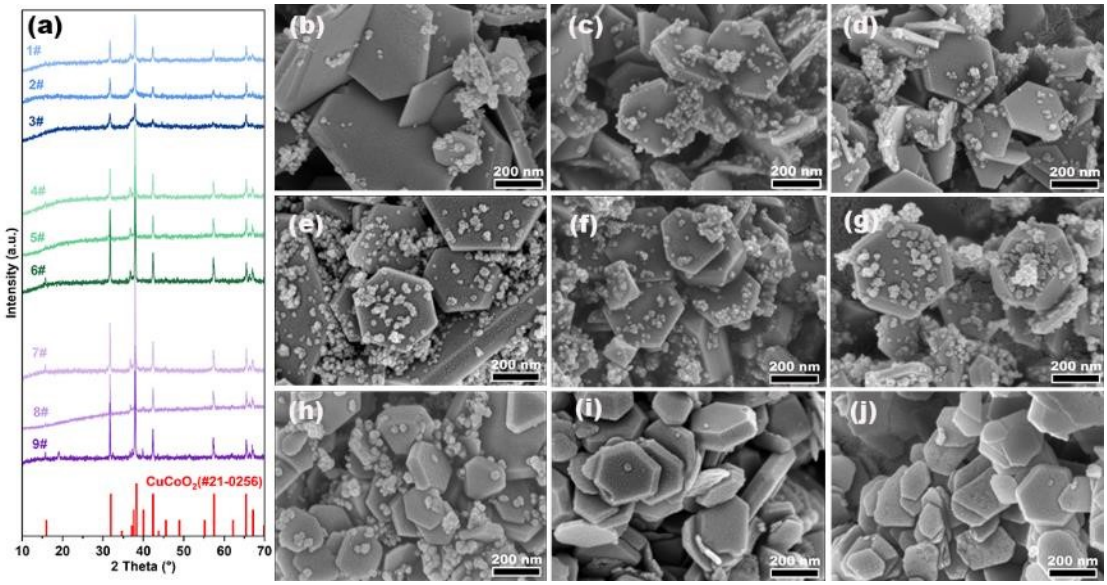

Fig. S1. XRD patterns (a) and SEM images (b, No. 1; c, No. 2; d, No. 3; e, No. 4; f, No. 5; g, No. 6; h, No. 7; i, No. 8; j, No. 9) of solvothermal reaction products.

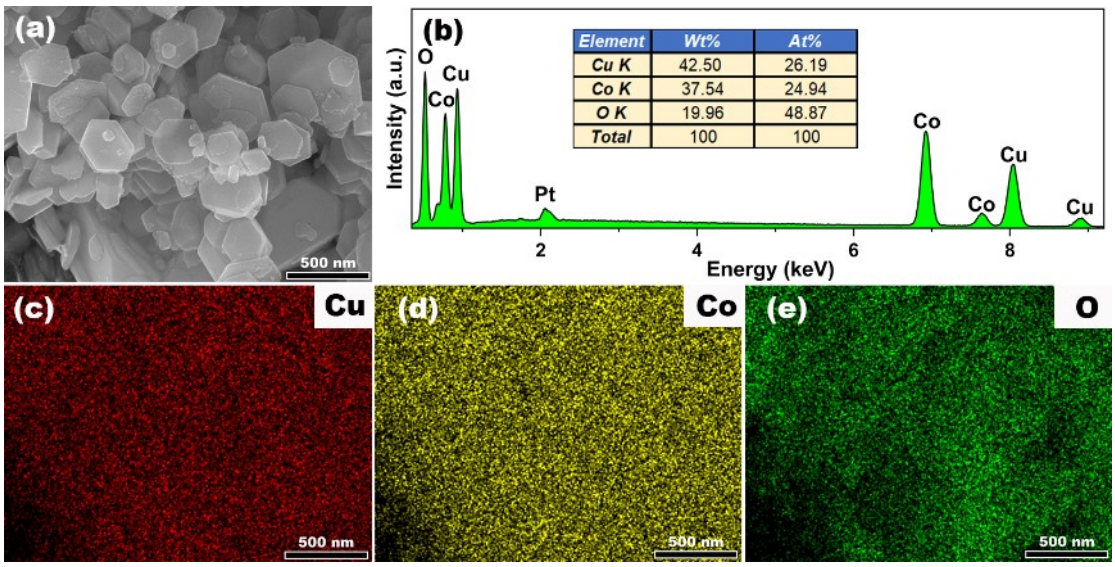

Fig. S2. SEM image (a), EDS spectrum (b) and elemental maps (c-e) of sample No. 8.

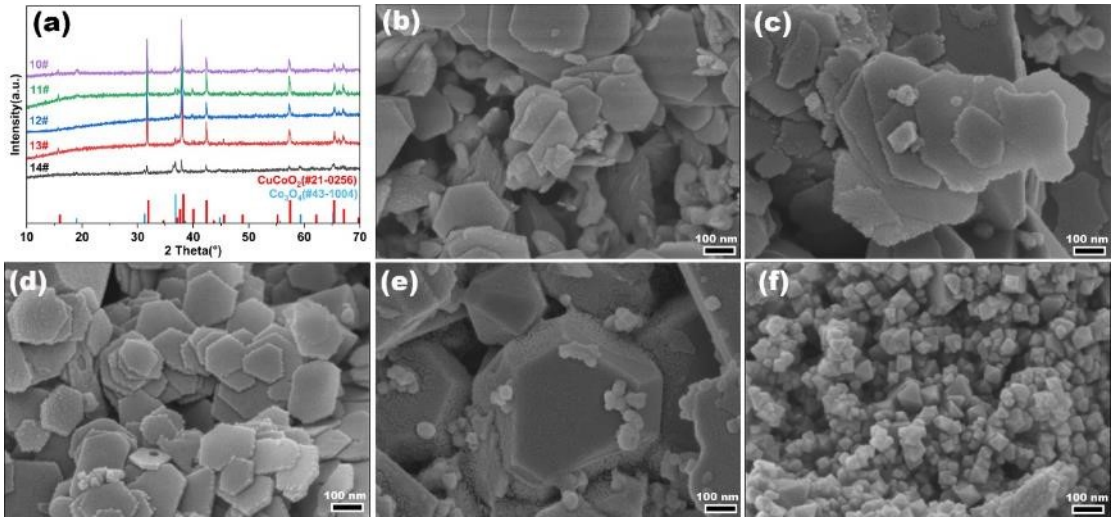

Fig. S3. XRD patterns (a) and SEM images (b, No. 10; c, No. 11; d, No. 12; e, 1 No. 3; f, No. 14) of solvothermal reaction products.

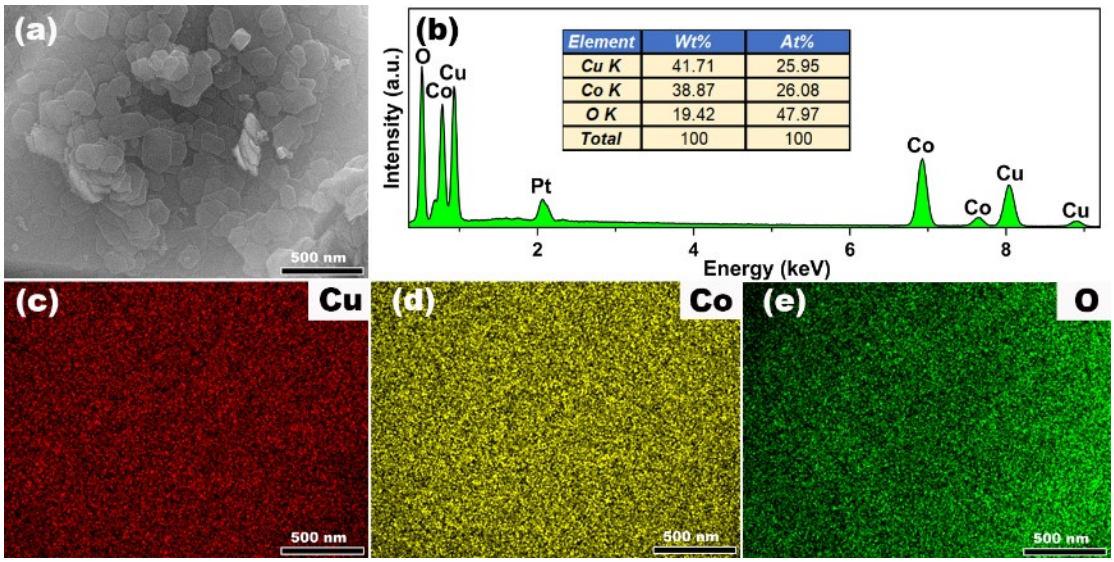

Fig. S4. SEM image (a), EDS spectrum (b) and elemental maps (c-e) of sample No. 12.

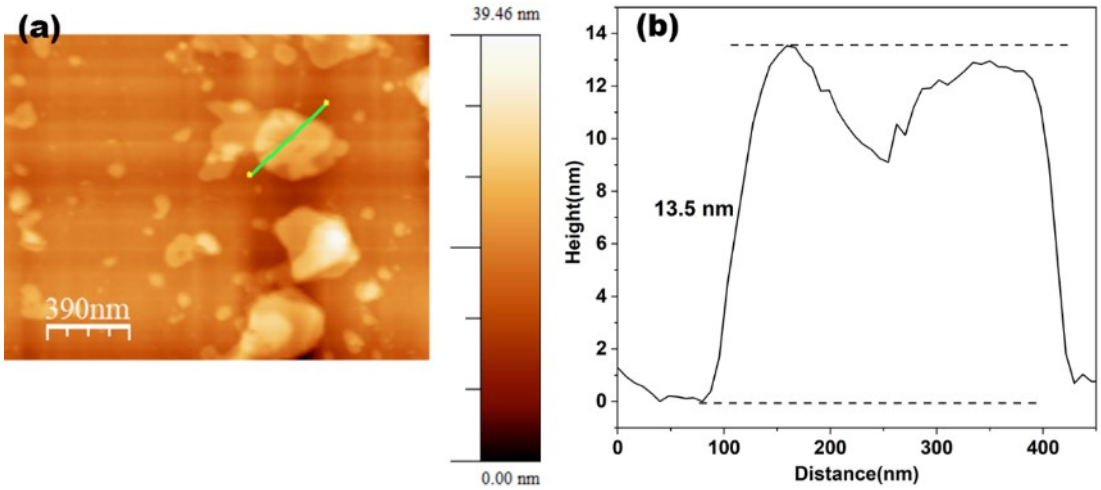

Fig. S5. AFM images (a) and the height profiles (b) of CCO2.

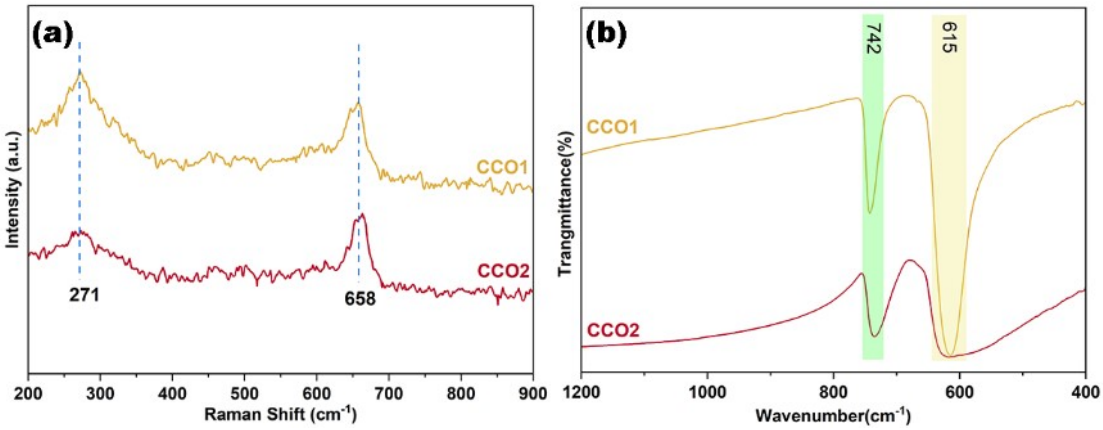

Fig. S6. The Roman spectra (a) and Fourier transform infrared spectra (b) of CCO1 and CCO2.

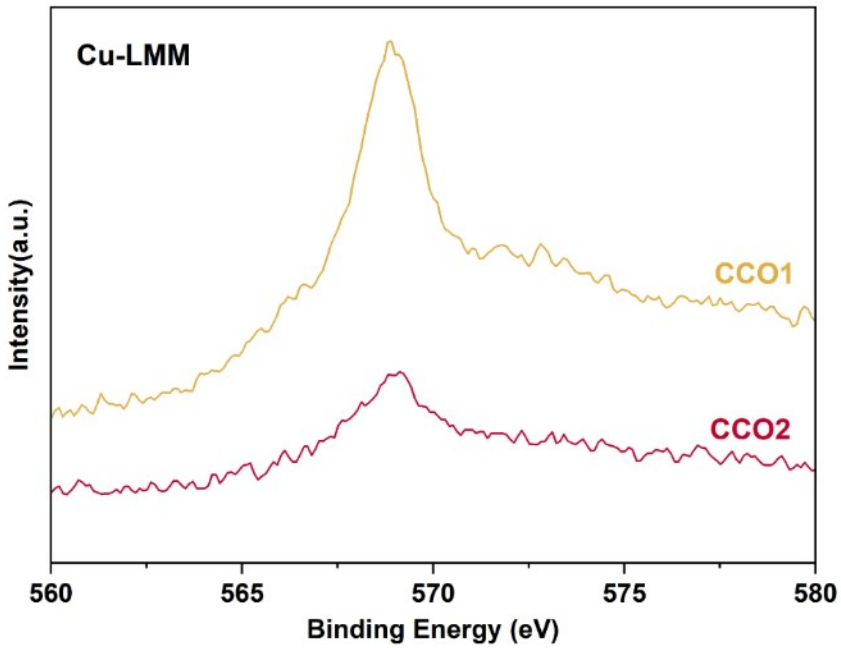

Fig. S7. The Cu-LMM Auger spectrum of CCO1 and CCO2.

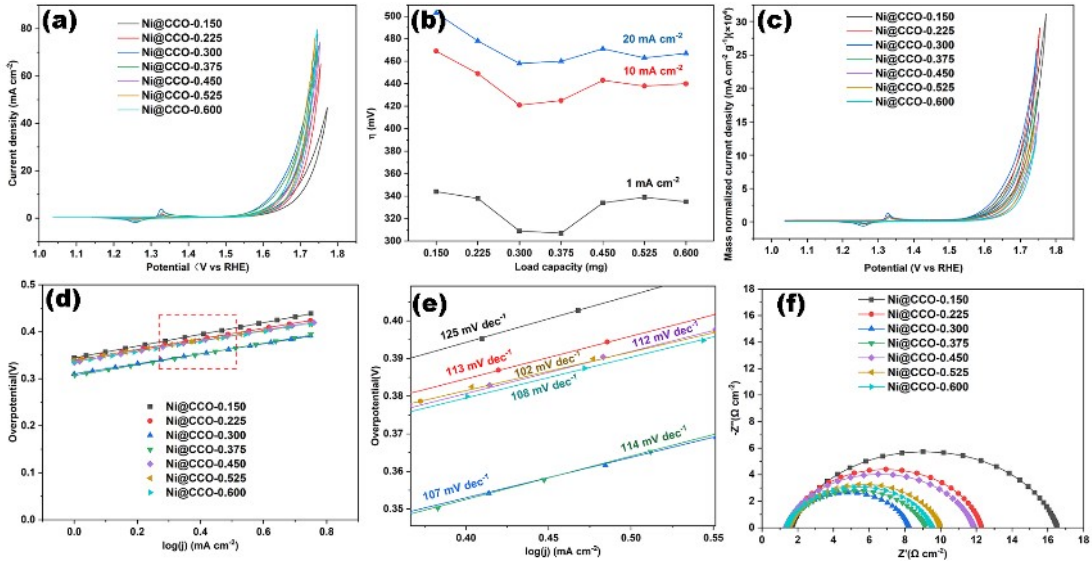

Fig. S8. The CV curves (a), the required overpotential at current densities of 1, 10 and 20 mA cm^{-2} (b), The CV curves (mass normalized current density) (c), Tafel plots (d), locally enlarged view of the Tafel slope (e) and electrochemical impedance spectrum (f) of working electrodes with different $CuCoO_2$ loading masss. The inset in (f) is the equivalent circuit mode.

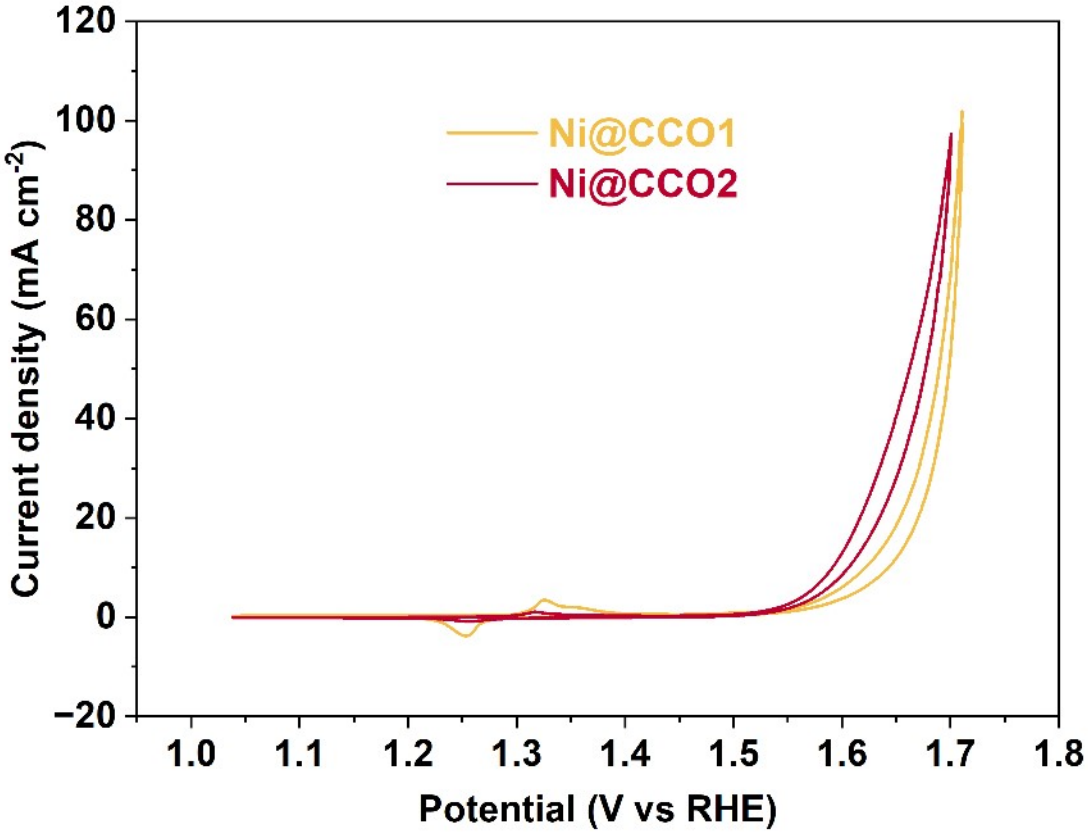

Fig. S9. CV curves (without iR loss compensation) of CCO1 and CCO2.

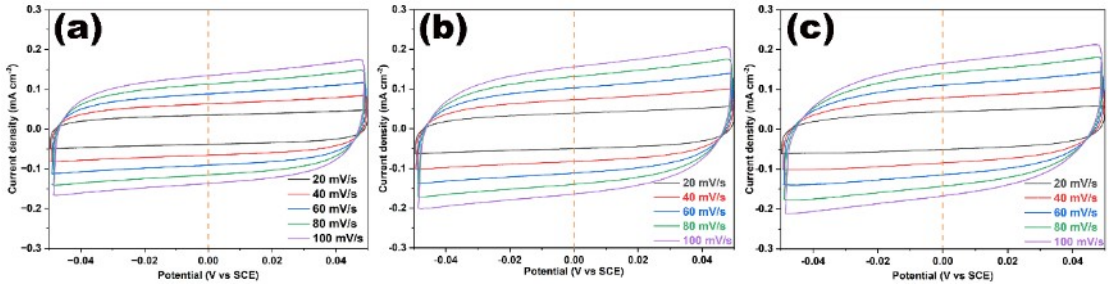

Fig. S10. CV curves of bare Ni (a), Ni@CCO1 (b) and Ni@CCO2 (c) at different sweep speeds (such as 20, 40, 60, 80, 100 mV/s).

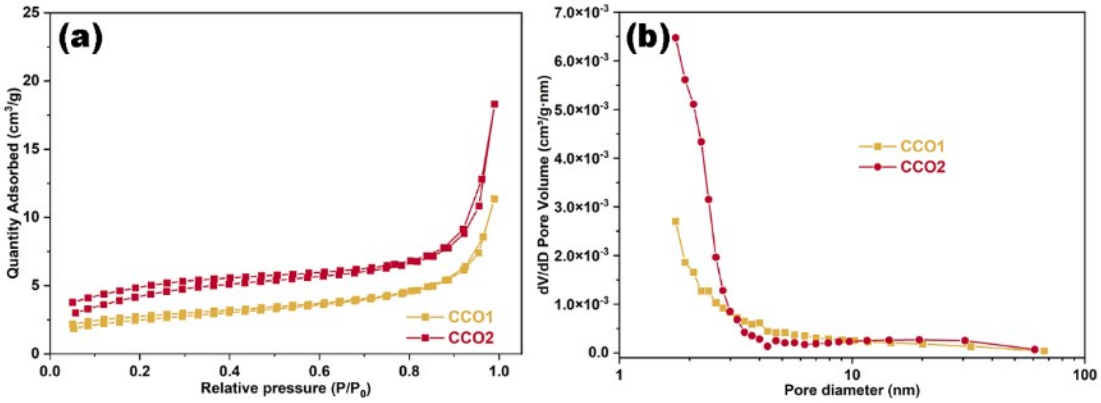

Fig. S11. N_2 adsorption-desorption isotherms (a) and pore structure (b) of CCO1 and CCO2.

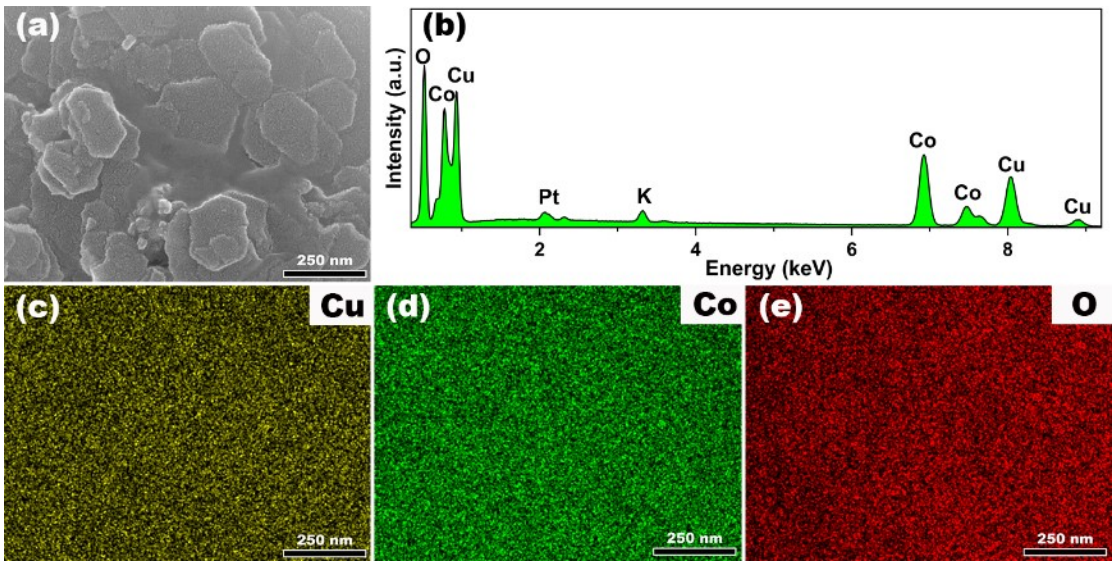

Fig. S12. SEM image (a), EDS spectrum (b) and elemental maps (c-e) of CCO2 after OER stability test.

References:

[1] Yang M, Tan H, Ma S, et al. Gram-scale Solvothermal Synthesis of Fe-doped $CuCoO_2$ Nanosheets and Improvement of Oxygen Evolution Reaction Performance[J]. *Nanoscale*, 2023, **15**(20), 12375-12387.

[2] Yang M, Han N, Shi L, et al. Effect of nickel doping on the structure, morphology and oxygen evolution reaction performance of Cu-BTC derived $CuCoO_2$[J]. *Dalton Transactions*, 2022, **51**(22): 8757-8765.

[3] Xiong D, Du Z, Li H, et al. Polyvinylpyrrolidone-assisted hydrothermal synthesis of $CuCoO_2$ nanoplates with enhanced oxygen evolution reaction performance[J]. *ACS Sustainable Chemistry & Engineering*, 2018, **7**(1): 1493-1501.

[4] Du Z, Qian J, Bai J, et al. Surfactant-modified hydrothermal synthesis of Ca-doped $CuCoO_2$ nanosheets with abundant active sites for enhanced electrocatalytic oxygen evolution[J]. *Inorganic Chemistry*, 2020, **59**(14): 9889-9899.

[5] Gao H, Yang M, Liu X, et al. Hydrothermal synthesized delafossite $CuGaO_2$ as an electrocatalyst for water oxidation[J]. *Frontiers of Optoelectronics*, 2022, **15**(1): 8.

[6] Zhang R, Sun Z, Zong C, et al. Increase of Co 3d projected electronic density of states in $AgCoO_2$ enabled an efficient electrocatalyst toward oxygen evolution reaction[J]. *Nano Energy*, 2019, **57**: 753-760.

[7] Moghaddam S K, Haghighi B, Ahmadian S M S, et al. Carbon paste electrode modified with $AgFeO_2$ as an electrocatalyst with excellent activity for water reduction and oxidation[J]. *Journal of Electroanalytical Chemistry*, 2019, **836**: 158-164.

[8] Liu C, Ji D, Shi H, et al. An A-site management and oxygen-deficient regulation strategy with a perovskite oxide electrocatalyst for the oxygen evolution reaction[J]. *Journal of Materials Chemistry A*, 2022, **10**(3): 1336-1342.

[9] Lu Y, Ma A, Yu Y, et al. Engineering oxygen vacancies into $LaCoO_3$ perovskite for efficient electrocatalytic oxygen evolution[J]. *ACS Sustainable Chemistry & Engineering*, 2018, **7**(3): 2906-2910.

[10] Dai J, Zhu Y, Zhong Y, et al. Enabling high and stable electrocatalytic activity of iron-based perovskite oxides for water splitting by combined bulk doping and morphology designing. *Advanced Materials Interfaces*, 2019, **6**(1): 1801317.

[11] Sun Y, Li R, Chen X, et al. A-site management prompts the dynamic reconstructed active phase of perovskite oxide OER catalysts[J]. *Advanced Energy Materials*, 2021, **11**(12): 2003755.